5. PURE STATES AND ENTANGLEMENT IN P@C_{60}

In was shown in chapter 3 that the large size of the ZFS parameter D of P@C_{60} in the rhombohedral crystal modification of in BrPOT allows selective pulsing on every ESR transition. Using this fact and the orientational dependence of the line separation open the way for basic quantum computation experiments. In this chapter, the experimental preparation and detection of pseudo-pure states and pseudo-entanglement in P@C_{60} in BrPOT will be presented. For these experiments special MW and RF pulse sequences were designed and implemented using a modified Bruker E680 W-band spectrometer of the Prof. Mehring's research group at the University of Stuttgart.

5.1 Preparation of Pseudo-pure States in P@C_{60} in BrPOT

A quantum mechanical system at normal conditions is in thermal equilibrium, which is actually a mixed state (see chapter 1.5.2). Every QC algorithm assumes a pure state before the calculation is started. This is an example of a non-equilibrium state for which there are several ways to prepare them experimentally. As a non-equilibrium state, this state will not last infinitely long, but for a limited time. For example, in ensemble quantum computers like bulk NMR the lifetime of a pure state cannot exceed T_1. In this particular experimental proposal they are called *pseudo-pure* states because strictly speaking they are not real pure states as pointed out in [20, 115, 116]. Nevertheless pseudo-pure states transform like pure states under unitary transformations and even QC algorithms can be experimentally implemented [20, 22].

An ensemble of spins in a constant magnetic field at thermal equilibrium is described by the Boltzmann density matrix (1.29). In order to prepare a pseudo-pure state some unitary transformation U_{pure} must be applied to (1.29), which can be experimentally realized by appropriate pulse sequences. The latter equalize the population of all states in the system except a single one, which is actually the desired pseudo-pure state.

The energy scheme of P@C_{60} in BrPOT consists of eight levels which are shown in Fig. 5.1a together with stick ESR (5.1b) and ENDOR (5.1c) spectra. Theoretically,

eight energy levels correspond to three qubits ($2^3 = 8$) but in this case not all the necessary transitions are allowed. Moreover, experimentally not all of the transitions can be excited simultaneously (both ESR and ENDOR) because of the limited frequency bandwidth[1] of the ENDOR resonator (see previous chapter). Therefore a subsystem of four levels (colored in blue in Fig. 5.1) belonging to different nuclear spin manifolds was chosen for the experiments. The position of the $|1\rangle \leftrightarrow |3\rangle$ ESR line depends on the orientation angle θ while the position of the $|4\rangle \leftrightarrow |6\rangle$ transition is fixed. In this way the line separation between these two in the ESR spectrum can be adjusted via the size of the ZFS term $D(\theta) = D(3\cos^2(\theta) - 1)$ in equation (3.2). The line separation must not be too small, otherwise selective excitation is not possible, thus $D(\theta) = 47$ MHz was chosen.

After the subsystem is selected and its transition frequencies adjusted the spin operators can be defined and then the pulse sequence for the preparation of pseudo-pure states have to be calculated. As all the pulses are transition selective, the fictitious spin 1/2 operators (section 1.5.5 in the introduction) for the subsystem are used. ρ_B is the initial state containing only diagonal elements (see equation (1.30)) where S_z for the whole system is written like:

$$S_z = (3/2, 3/2, \mathbf{1/2}, 1/2, \mathbf{\text{-}1/2}, \mathbf{\text{-}1/2}, -3/2, \mathbf{\text{-}3/2}) \tag{5.1}$$

The elements that are part of the truncated initial density matrix are given in bold. According to equation (1.30) ρ_B is:

$$\rho_B = \frac{\mathbb{1}}{8} - \alpha S_z = \mathbb{1}\left(\frac{1}{8} + \frac{5}{6}\alpha\right) - \alpha\left(\frac{5}{6}\mathbb{1} + Sz\right) = \mathbb{1}\left(\frac{1}{8} + \frac{5}{6}\alpha\right) + \alpha\widetilde{\rho_B} \tag{5.2}$$

The calculation of the all pulse sequences were done using $\widetilde{\rho_B}$. For each of the three allowed transitions (two ESR and one ENDOR) the three fictitious spin 1/2 operators S_x^{nm}, S_y^{nm} and S_z^{nm} are defined, where n and m denote the energy levels (see chapter 1.5.5). The matrices of each operator contain $8 \times 8 = 64$ elements but only two of them are non-zero. As an example the full matrix of S_x^{13} operator is

[1] The measured bandwidth was about 100 MHz ($\approx$ 35.71 G), meaning that if two lines are separated in the ESR spectrum by more than 100 MHz, they cannot be excited simultaneously without significant loss of signal.

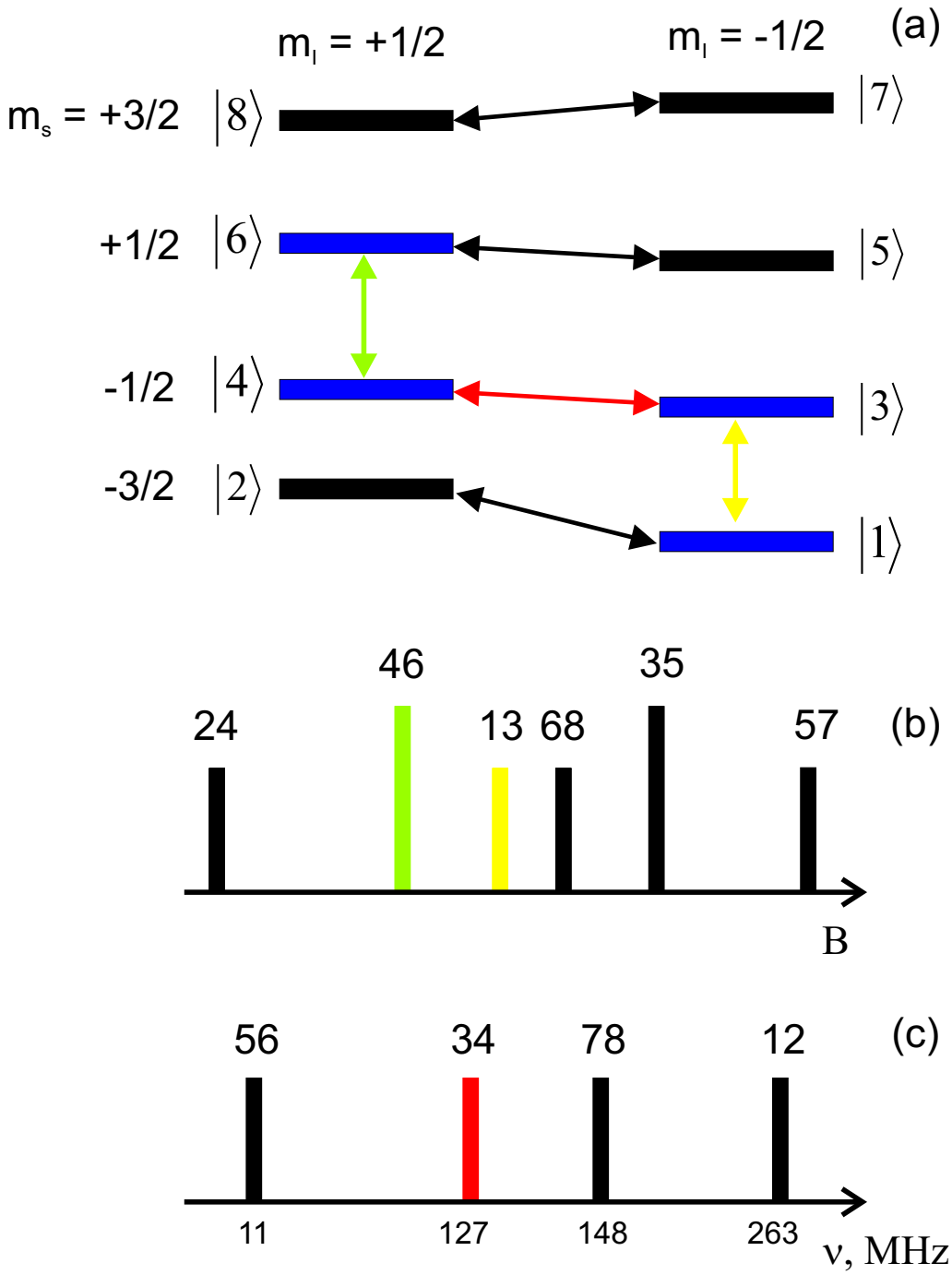

Fig. 5.1: Energy levels of P@C_{60} in BrPOT (a), the ESR spectrum for the used orientation (b) and the ENDOR spectrum. The four levels of the first subsystem are marked in blue, the ESR transitions in yellow and brown and (c) the ENDOR transition is shown in red.

given:

$$S_x^{13} = \begin{pmatrix} 0 & 0 & 0 & 0 & 0 & 0 & 0 & 0 \\ 0 & 0 & 0 & 0 & 0 & 0 & 0 & 0 \\ 0 & 0 & 0 & 0 & 0 & 0 & 0 & 0 \\ 0 & 0 & 0 & 0 & 0 & 0 & 0 & 0 \\ 0 & 0 & 0 & 0 & 0 & 0 & 0 & 0 \\ 0 & 0 & 0 & 0 & 0 & 0 & 0 & \frac{1}{2} \\ 0 & 0 & 0 & 0 & 0 & 0 & 0 & 0 \\ 0 & 0 & 0 & 0 & 0 & \frac{1}{2} & 0 & 0 \end{pmatrix} \tag{5.3}$$

The density matrices (in the subsystem) of the pseudo-pure states ρ_6 and ρ_4 are:

$$\rho_6 = \begin{pmatrix} 1 & 0 & 0 & 0 \\ 0 & 0 & 0 & 0 \\ 0 & 0 & 0 & 0 \\ 0 & 0 & 0 & 0 \end{pmatrix}; \quad \rho_4 = \begin{pmatrix} 0 & 0 & 0 & 0 \\ 0 & 1 & 0 & 0 \\ 0 & 0 & 0 & 0 \\ 0 & 0 & 0 & 0 \end{pmatrix} \tag{5.4}$$

Only the states $|6\rangle$ ($|4\rangle$) are populated and all others in the subsystem are "empty". It is clear that the Boltzmann density matrix $\widetilde{\rho_B}$ can be transformed to ρ_6, ρ_4 respectively, with the appropriate propagator:

$$\rho_6 = U_6.\widetilde{\rho_B}.U_6^\dagger \quad \rho_4 = U_4.\widetilde{\rho_B}.U_4^\dagger \tag{5.5}$$

with $U_6 = e^{-i\beta_2 I_x^{34}} e^{-i\beta_1 S_x^{13}}$ for the preparation of ρ_6, $U_4 = e^{-i\beta_3 S_x^{46}} U_6$ for ρ_4 using rotating angles $\beta_1 = \arccos(-1/3)$ ($\approx 109°$), $\beta_2 = \pi/2$ and $\beta_3 = \pi$. Experimentally, U_6 is realized as an MW pulse $P_x^{13}(109°)$ followed by an RF pulse $P_x^{34}(\pi/2)$. The preparation and detection pulse sequences are depicted in Fig. 5.2. There is a time delay between the pulses to assure that the transverse components have decayed. For the implementation of U_4, a third MW pulse $P_x^{46}(\pi)$ is applied after these two pulses to transfer the population from $|6\rangle$ to $|4\rangle$. The preparation pulses equalize the population of all energy levels except the level that corresponds to the desired pure state ($|6\rangle$ or $|4\rangle$).

The pulse sequences described above prepare the two pseudo-pure states, which must be detected to prove their existence. For this purpose the elements of the density matrix must be measured, which is done by *density matrix tomography* [117, 118, 119]. Depending on the quantum mechanical system to be analyzed, different pulse sequences are applied. Let some pulse sequence be applied to an ensemble of non-

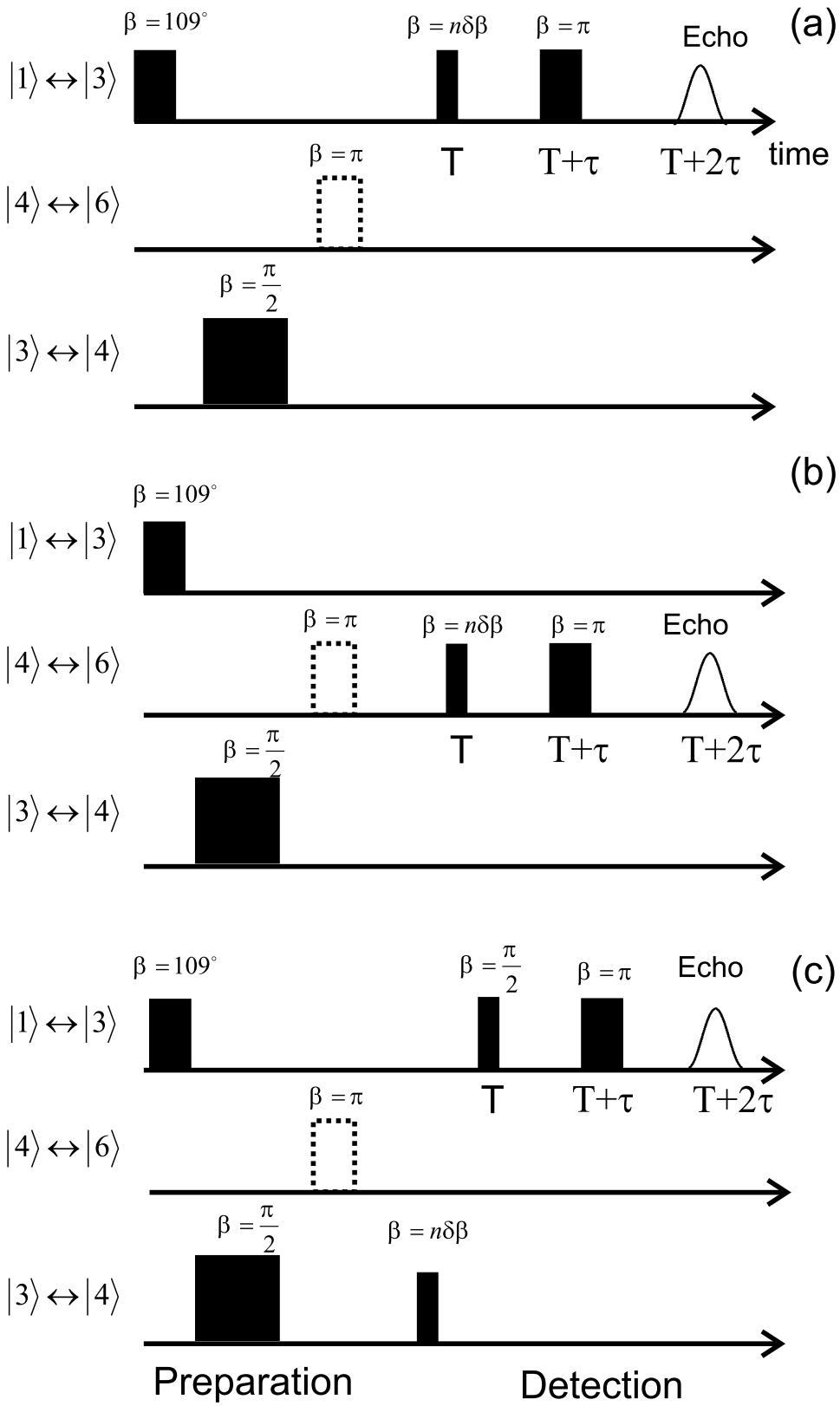

Fig. 5.2: Pulses sequences for the preparation and detection of the pseudo-pure state ρ_6. For ρ_4 a π pulse on the transition $|3\rangle \leftrightarrow |4\rangle$ must be added (denoted with dashed line). Rabi oscillations are done between the transitions $|1\rangle \leftrightarrow |3\rangle$ (a), $|4\rangle \leftrightarrow |6\rangle$ (b) and $|3\rangle \leftrightarrow |4\rangle$ (c).

interacting electrons creating the density matrix (compare to equation (1.23)):

$$\rho = \begin{pmatrix} p_1 & p_{12} \\ p_{21} & p_2 \end{pmatrix} \tag{5.6}$$

The detection of the elements can be realized with Rabi oscillations on the transition $|+1/2\rangle \leftrightarrow |-1/2\rangle$. The amplitude of the latter will give $p_{11} - p_{22}$ as the signal is proportional to the population difference. Together with the condition $tr(\rho) = 1$ the diagonal elements can be easily calculated. For this experiment the off-diagonal elements must be zero, meaning that the detection must be applied at time T_m after the preparation pulses. To measure the off-diagonal elements of the density matrix, the time delay between preparation and detection sequence must be minimized (ideally zero).

For tomography ρ_6 and ρ_4 only the diagonal elements were determined measuring Rabi oscillations on all three transitions. The amplitude of the first period in the Rabi oscillations determines the population difference between the levels connected by the transition. As there are four diagonal elements but only three experimental amplitudes, the normalizing condition 1.24 is added to obtain the following set of equations:

$$p_1 - p_3 = A_{13} \tag{5.7}$$

$$p_3 - p_4 = A_{34} \tag{5.8}$$

$$p_4 - p_6 = A_{46} \tag{5.9}$$

$$p_1 + p_3 + p_4 + p_6 = 1 \tag{5.10}$$

here A_{nm} are the amplitudes of the first Rabi oscillations between the transition $|n\rangle \leftrightarrow |m\rangle$ and $p_i \equiv \rho_{ii}$ are the diagonal elements of the density matrix. The intensity of the detected signal is normalized to the Rabi oscillations of the Boltzmann equilibrium or in other words when only the detection pulse sequence is applied. The time traces of the raw signals (only with baseline corrections) for ρ_6 and ρ_4 are shown in Fig. 5.3 and 5.4 respectively. The decay of the signal is caused by inhomogeneities in the magnetic component B_1 of the MW pulse. It is worth noting the much smaller signal and inverted phase of the first Rabi oscillation when the transition used for the detection does not involve the pure state prepared (Fig. 5.3 top) compared to the other ESR transition (Fig. 5.3 bottom). Ideally, no signal should be detected but the non-ideal pulse length causes its appearance. Inversion of the first oscillation occurs because the 109° MW pulse rotates the spin ensemble partially in the $-z$ axis and there are components on the x and y axis. The

same inversion is observed when ρ_4 is prepared and the transition $|4\rangle \leftrightarrow |6\rangle$ is used (Fig. 5.4 middle) which is to be expected as the spin polarization is transferred with the $P_x(\pi)$ pulse from $|6\rangle$ to $|4\rangle$ (Fig. 5.2). No ENDOR effect from the transition $|3\rangle \leftrightarrow |4\rangle$ could be observed in the detection of ρ_4 meaning that the populations of these two levels are equalized and the pure state is well prepared. In contrast there is a strong ENDOR signal from the same transition if ρ_6 is created as shown in Fig. 5.3 (bottom). Unfortunately the RF coil in the ENDOR resonator is not able to provide large magnetic fields (B_2) so that the length of the RF π pulse was about 60 μs. Therefore only a half period of the first Rabi oscillation could be measured before the maximal possible pulse length was reached. Nevertheless the first maximum is clearly seen and the population difference could be measured. Solving equations (5.10) gives the following density matrix for the two pure states:

$$\rho_6^{exp} = \begin{pmatrix} 0.96 & 0 & 0 & 0 \\ 0 & 0.00 & 0 & 0 \\ 0 & 0 & 0.00 & 0 \\ 0 & 0 & 0 & 0.04 \end{pmatrix} \tag{5.11}$$

$$\rho_4^{exp} = \begin{pmatrix} -0.02 & 0 & 0 & 0 \\ 0 & 0.98 & 0 & 0 \\ 0 & 0 & -0.01 & 0 \\ 0 & 0 & 0 & 0.03 \end{pmatrix} \tag{5.12}$$

The deviation of the values of the matrix elements from the theoretical values (equation (5.4)) is due to imperfect pulses (both RF and MW) and the error is about 4 %. The negative values of some elements do not mean negative population, which does not have any physical meaning, but negative deviation from the equalized population of the levels because these are pseudo-pure state and not real pure states.

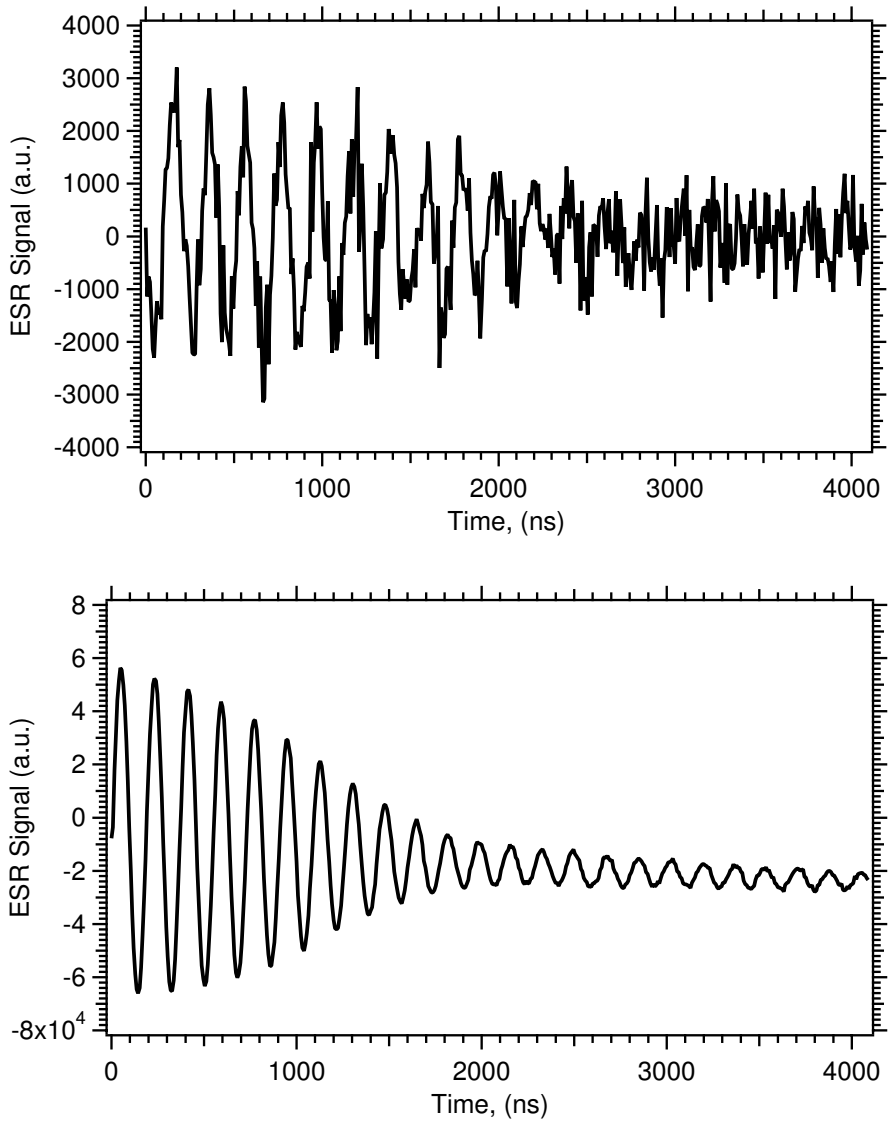

Fig. 5.3: Rabi oscillations of the transitions $|1\rangle \leftrightarrow |3\rangle$ (top) and $|4\rangle \leftrightarrow |6\rangle$ (bottom) for the tomography of the density matrix ρ_6. The levels $|3\rangle$ and $|4\rangle$ are equally populated and no Rabi oscillations could be measured.

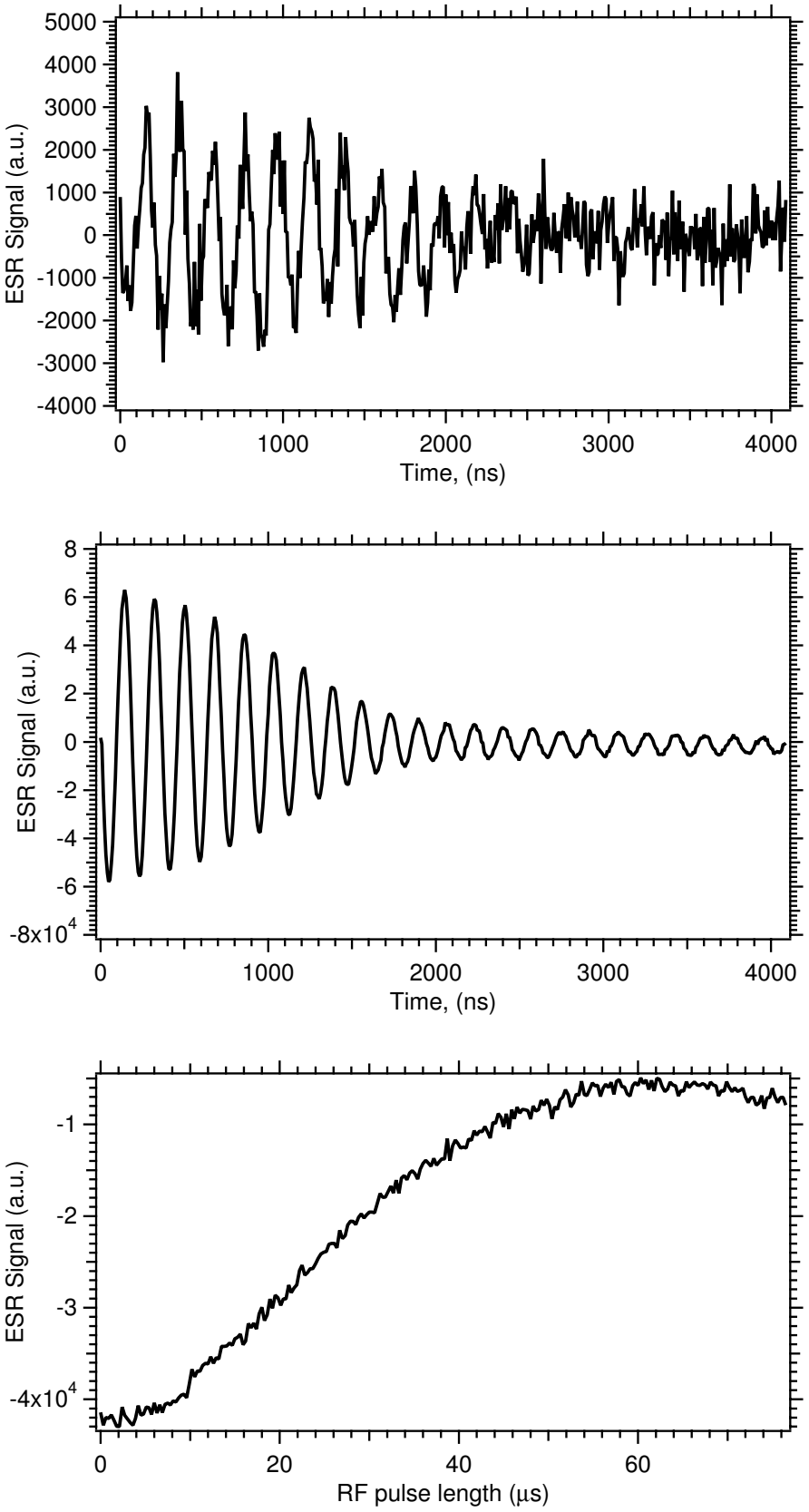

Fig. 5.4: Rabi oscillations of the transitions $|1\rangle \leftrightarrow |3\rangle$ (top), $|4\rangle \leftrightarrow |6\rangle$ (middle) and $|3\rangle$ and $|4\rangle$ (bottom) for the tomography of the density matrix ρ_4.

5.2 Phase Rotations

The technique of pulse phase rotation will be briefly described as it will be used later to detect the prepared entangled state. The MW pulses in the sequences used in the previous chapters (and in the almost all of the ESR pulse experiments) were either in phase with each other or had a constant phase shift, for example in the CPMG sequence there is a 90° shift in the phase of the MW frequency of the first $\pi/2$ pulse compared to the train of π pulses. Sometimes phase cycling was applied in order to reduce the signal of unwanted FIDs and echoes, i.e. the relative phase of the pulses was changed (by 90°, 180° or 270°) in a number of experiments and the signals were added accordingly. Generally the phase of the MW frequency can be chosen arbitrarily, but all modern pulse ESR spectrometers use pulse channels with fixed phase shift. A pulse with arbitrary phase ϕ and rotation angle β will be written as $P_{\phi}^{nm}(\beta)$ where nm denotes the transition (ESR or ENDOR) and the corresponding propagator is [33]:

$$P_{\phi}^{nm}(\beta) = e^{-i\phi S_z^{nm}} e^{-i\beta S_x^{nm}} e^{i\phi S_z^{nm}} \tag{5.13}$$

For example an x pulse with phase $\phi = 0$ is still an x pulse. For $\phi = \pi/2$ according to equation (5.13) the x pulse transforms to a y pulse:

$$P_{\pi/2}^{nm}(\beta) = e^{-i\frac{\pi}{2}S_z^{nm}} e^{-i\beta S_x^{nm}} e^{i\frac{\pi}{2}S_z} = e^{-i\beta S_y^{nm}} \tag{5.14}$$

The continuous variation of the phase of a pulse is called *phase rotation* [118, 119] which is actually a rotation of the electron (nuclear) spin around the z-axis. The latter is mathematically described by the following unitary transformation of the spin states (in Hilbert space):

$$U_S|m_s\rangle = e^{-i\phi_E S_z}|m_s\rangle = e^{-im_s\phi_E}|m_s\rangle \tag{5.15}$$

here S_z is the electron spin z operator, m_s is the electron spin quantum number and ϕ_E is the phase increment. For nuclear spins m_s and S_z should be replaced with m_I and I_z. Pulsed ESR spectrometers can record data only as a time trace or as a magnetic field sweep so the phase increment must be converted into a fictitious time increment according to the expression:

$$\delta\phi_E = 2\pi\nu_E\delta t \tag{5.16}$$

where ν_E is called *phase frequency* and $\delta\phi$ is the *Time Proportional Phase Increment* (TPPI) [120]. The phase frequency is arbitrarily chosen in the experiments

by adjusting the step size of the phase increments.
The phase rotations were implemented in a W-band spectrometer where the phase of the MW pulses were changed at 9 GHz and then converted to 94 GHz. A polycrystalline sample of $^{15}N@C_{60}$ was chosen for the first tests as it has good ESR and ENDOR signals at room temperature. The pulse sequences used were a modified Hahn echo for the electron spin (Fig. 5.5a) and Mims ENDOR (Fig. 5.5b). The time traces are shown in Fig. 5.6 where the oscillations are clearly seen and the frequencies are determined by equation (5.16).

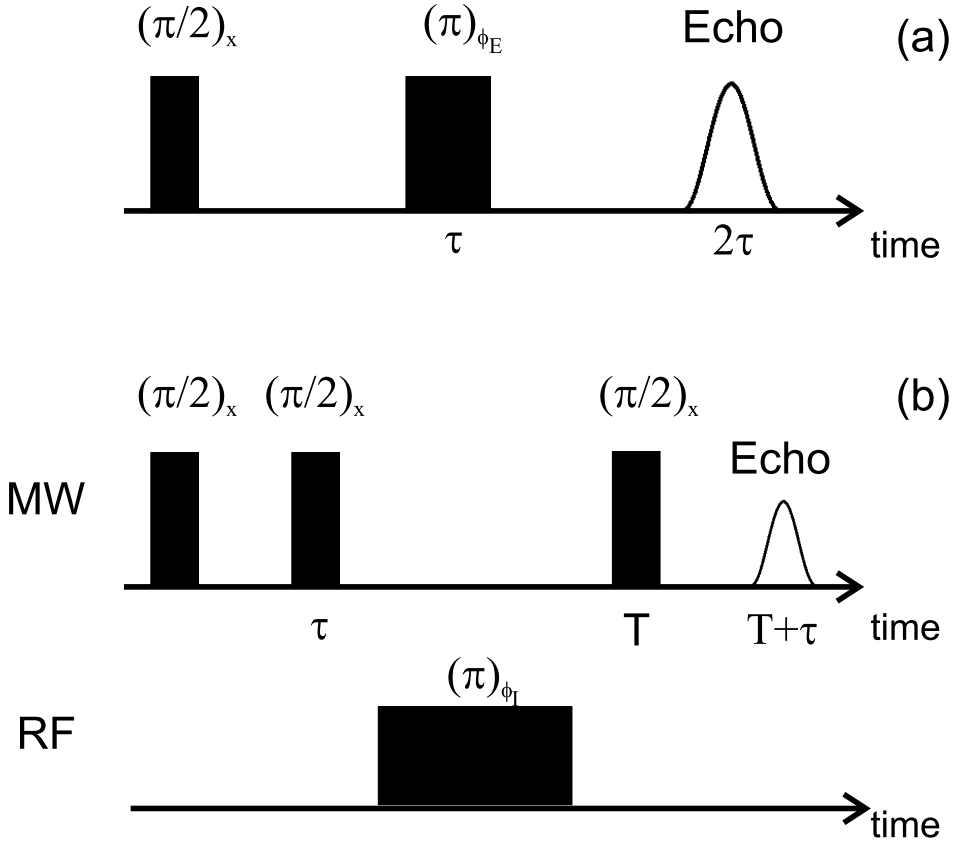

Fig. 5.5: Modified Hahn echo (a) and Mims ENDOR (b) pulse sequences. The subscript x denotes that these are usual x pulses, ϕ_E and ϕ_I are the electron and nuclear spin phase increments.

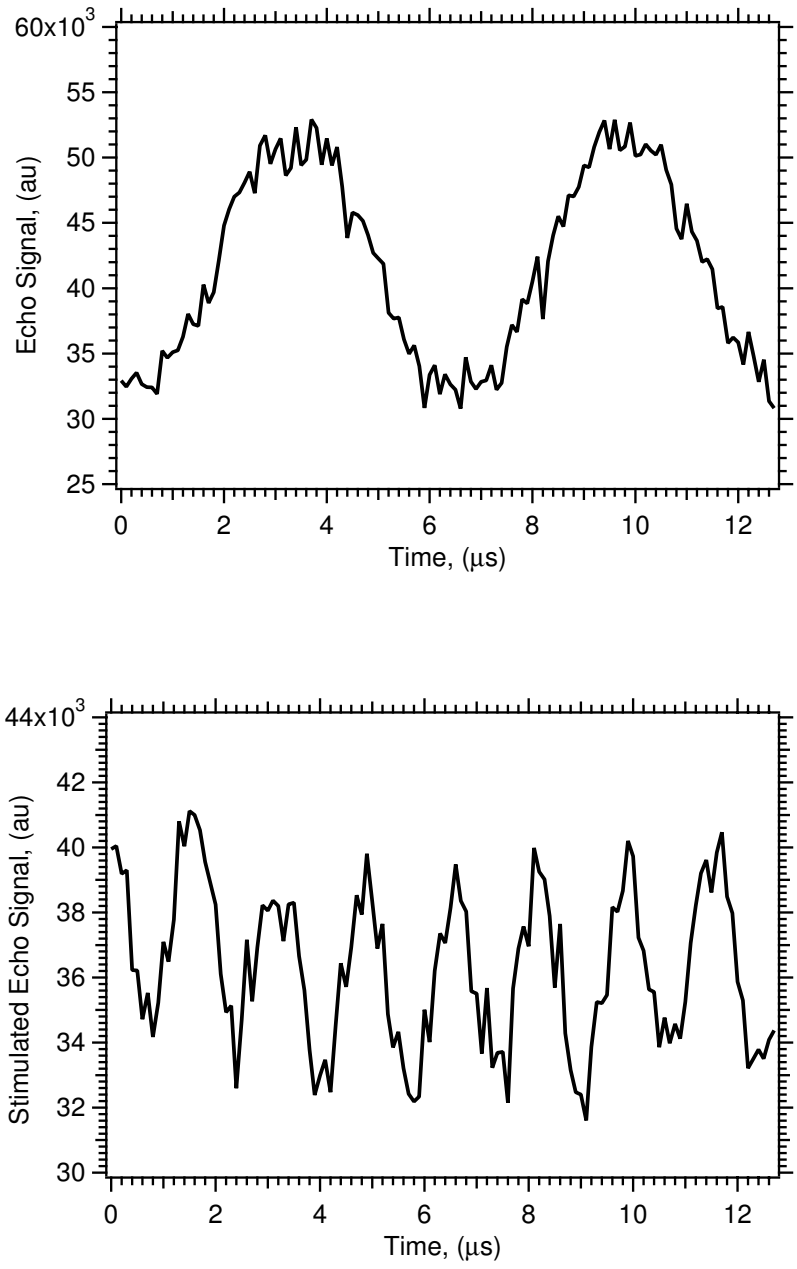

Fig. 5.6: Time traces of the electron spin (top) and nuclear spin (bottom) phase rotations in $^{15}N@C_{60}$.

5.3 Pseudo-Entanglement in P@C_{60} in BrPOT

Entanglement is one of the most striking counter intuitive phenomena in quantum mechanics and some of its peculiar properties were already mentioned in the introduction (see chapter 1.3).
An entangled state is written in the form of equation (1.5) and for the density matrix of the subsystem from Fig. 5.2 it looks like:

$$\rho_{ent} = \begin{pmatrix} 0 & 0 & 0 & 0 \\ 0 & \frac{1}{2} & 0 & \frac{1}{2} \\ 0 & 0 & 0 & 0 \\ 0 & \frac{1}{2} & 0 & \frac{1}{2} \end{pmatrix} \tag{5.17}$$

The entanglement is between the states $|4\rangle$ and $|1\rangle$ and analogous to equation (1.5) $|\phi_{ent}\rangle$ is written like:

$$|\phi_{ent}\rangle = \frac{1}{\sqrt{2}}(|1\rangle + |4\rangle) = \frac{1}{\sqrt{2}}(|\uparrow\downarrow\rangle + |\downarrow\uparrow\rangle) \tag{5.18}$$

$|\uparrow\rangle$ denotes nuclear (electron) spin up and the $|\downarrow\rangle$ denotes spin-down. This state can be prepared using the unitary transformation U_{ent} applied to the pure state ρ_4

$$U_{ent} = e^{-i\frac{\pi}{2}I_x^{34}} e^{-i\pi S_x^{13}} \tag{5.19}$$

so that:

$$\rho_{ent} = U_{ent}.\rho_4.U_{ent}^{\dagger} \tag{5.20}$$

is fulfilled. The experimental realization of U_{ent} is a $\pi/2$ RF pulse on transition $|3\rangle \leftrightarrow |4\rangle$ followed by a π pulse on the ESR transition $|1\rangle \leftrightarrow |3\rangle$, both applied after the preparation of ρ_4. The initial state for the entanglement is pseudo-pure hence pseudo-entanglement is created the presence of which must be confirmed. The detection is implemented as a back transformation of the entanglement with the unitary transformation:

$$U_{BT} = P_{\phi_2}^{13}(\frac{\pi}{2})P_{\phi_1}^{34}(\pi) = e^{-i\phi_2 S_z^{13}} e^{-i\pi S_x^{13}} e^{i\phi_2 S_z^{13}} e^{-i\phi_1 I_z^{34}} e^{-i\frac{\pi}{2}I_x^{34}} e^{i\phi_1 I_z^{34}} \tag{5.21}$$

where ϕ_1 and ϕ_2 are the nuclear and electron spin phase increments respectively. The application of U_{BT} on ρ_{ent} would result in the following expectation value for $\langle S_z\rangle$:

$$\langle S_z\rangle = Tr(S_z U_{BT}\rho_{ent}U_{BT}^{\dagger}) = 2 - \frac{1}{4}\cos(\phi_1 + \phi_2)) \tag{5.22}$$

$\langle S_z \rangle$ is detected by Hahn echo sequence.
The complete pulse sequence is depicted in Fig. 5.7. Equation (5.22) shows that that

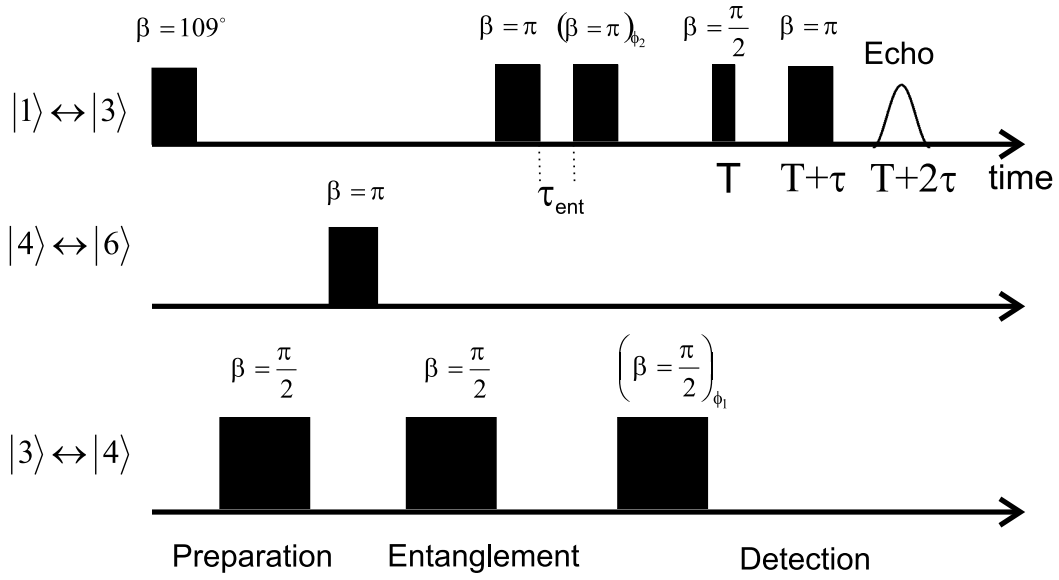

Fig. 5.7: Pulse sequence for the creation and detection of entanglement between states $|1\rangle$ and $|4\rangle$. The phase increments of the RF and MW pulses are denoted with ϕ_1 and ϕ_2, respectively.

the echo signal from the back transformation of the entangled state will oscillate with the single frequency $\nu_{ent} = \nu_E + \nu_I$, which is the sum of both nuclear and electron spin phase frequencies. They are connected with the phase increments ϕ_1 and ϕ_2 according to equation (5.16). If the two states are not entangled then the two individual frequencies would be measured. The experimental phase oscillation of the entangled state and its Fourier transformation are shown in Fig. 5.8. The major peak corresponds to the sum of the two phase frequencies of the nuclear and electron spin $\nu_{ent} = 1.525$ MHz but also small peaks at the individual frequencies ν_E (0.625 MHz) and ν_I (0.9 MHz) are observed although with much smaller amplitude. Thus the unitary transformation U_{ent} indeed creates an entangled state and with the back transformation U_{BT} the detection is successful and the signal follows equation (5.22). The fact that additional peaks of the individual phase rotations appear in the power spectrum is ascribed mainly to decoherence and imperfections of the both RF and MW pulses despite the careful optimization of their length. Here, the fidelity of the prepared entanglement will be defined as:

$$F = \frac{A_{\nu_E+\nu_I}}{A_{\nu_E} + A_{\nu_I} + A_{\nu_E+\nu_I}} \tag{5.23}$$

where A_i is the area of peak i in the Fourier transform and F is the fidelity for which $0 \leq F \leq 1$ is fulfilled. From the above equation fidelity $F = 0.911$ is calculated.

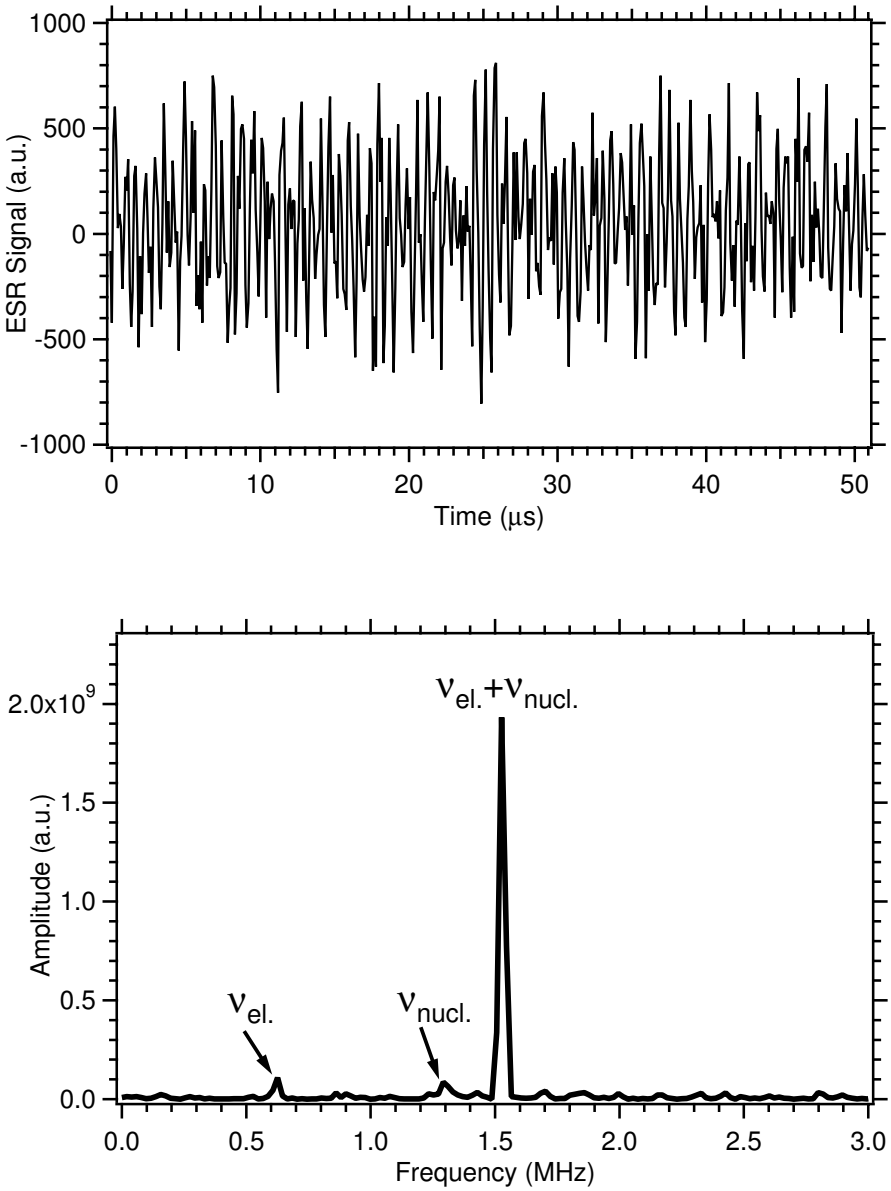

Fig. 5.8: Phase oscillation for the detection of the entanglement (top) and the power spectrum after the Fourier transform of the time trace (bottom). Small peaks at $\nu_E = 625$ kHz and $\nu_I = 900$ kHz are observed together with the main peak $\nu = \nu_E + \nu_I = 1.525$ MHz. The fidelity of the entanglement is $F = 0.911$

The delay τ_{ent} between the creation and detection of the entanglement was set to 30 ns which is much shorter than the electron coherence time $T_m = 12\ \mu$s at that temperature ($T = 25$ K). To test whether imperfect pulses or decoherence cause the incomplete entanglement τ_{ent} was increased to 130 ns. The Fourier transformation of the resulting phase oscillation is shown in Fig. 5.9. The decrease of the peak at ν_{ent} compared to those at ν_E and ν_I is evidence for a fast collapse of the entanglement and proves that the presence of ν_E and ν_I in Fig. 5.8 is due to decoherence of the entanglement, possibly already during the pulses. This fact is quite astonishing as it seems that the life time of the entanglement is much shorter than the electron coherence time. Another possibility is that the observed decay is caused by magnetic inhomogeneities in the crystal, in other words it is the "FID" of the entanglement. Then, theoretically, it could be refocused similar to the refocusing of the magnetization by the π pulse in the Hahn echo experiment. In this case the population of the states $|1\rangle$ and $|4\rangle$ must be exchanged and a pulse sequence consisting of RF and MW pulses could be easily calculated. Unfortunately, the coherence time of the ESR transitions T_2^{ESR} are much shorter than the length of the RF pulse t_p^{RF} meaning that during the RF pulse the coherence will be completely destroyed as $t_p^{RF} \approx 3T_2^{ESR}$. Hence no refocusing is possible in this case. The decoherence of the entanglement will be investigated in more detail in the next section.

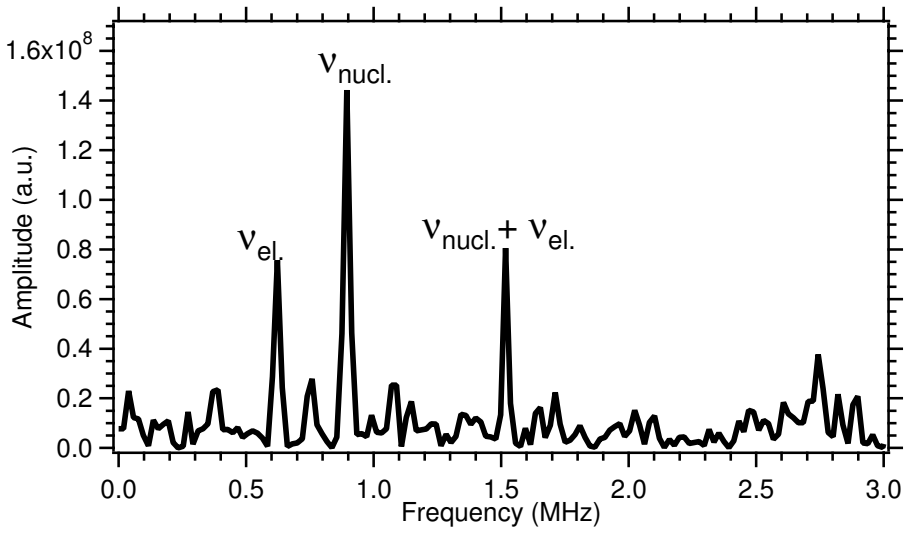

Fig. 5.9: Fourier transformation of the phase oscillation using the pulse sequence shown in Fig. 5.7 with $\tau_{ent} = 130$ ns. The almost complete collapse of the entanglement is clearly seen. The calculated fidelity in this case is $F = 0.758$.

5.4 Decoherence of the pseudo-entanglement

The short lifetime of the entanglement raises the question whether it can be prolonged when other states of the system are used to create an entangled state instead of those used in the previous section - $|1\rangle$ and $|4\rangle$. These states belong to ESR transitions with different Rabi frequencies and different electron coherence times T_m for the transition $|1\rangle \leftrightarrow |3\rangle$ $T_m^{13} = 18\ \mu$s ($m_s = +1/2 \leftrightarrow m_s = -3/2$) and for $|4\rangle \leftrightarrow |6\rangle$ $T_m^{46} = 12\ \mu$s ($m_s = -1/2 \leftrightarrow m_s = -1/2$). One possibility would be to define a subsystem of four states with magnetic quantum number $|m_s| = 3/2$ as these transitions have longer T_m (for example $|1\rangle$, $|2\rangle$,$|3\rangle$ and $|4\rangle$). This can however not be achieved experimentally because both the separation of the spectral lines is larger than the resonator bandwidth and there is no suitable ENDOR transition. Another possibility is to entangle two levels which have $|m_S| = 1/2$ as their energy does not depend on the size (and correspondingly on the fluctuations) of the ZFS parameter. A new subsystem was defined consisting of the states $|2\rangle$, $|3\rangle$, $|4\rangle$ and $|5\rangle$ (Fig. 5.10) and the optimal line separation was adjusted by rotation of the crystal. In analogy with equation (5.1) the S_z operator of the system is given, where the levels of the new system are given in bold:

$$S_z = (3/2, 3/2, 1/2, \mathbf{1/2}, \mathbf{\text{-}1/2}, \mathbf{\text{-}1/2}, \mathbf{\text{-}3/2}, -3/2) \tag{5.24}$$

After the proper orientation of the sample is found again, the necessary pseudo-pure states must be prepared, which now are ρ_2 and ρ_4. The propagators are the same as those used for ρ_4 and ρ_6 but the fictitious spin 1/2 operators should be changed for the corresponding transition. Hence the unitary transformations are:

$$U_2 = e^{-i\beta_1 S_x^{35}} e^{-i\beta_2 I_x^{34}} \quad U_{4b} = e^{-i\beta_3 S_x^{24}} U_2 \tag{5.25}$$

so that, in analogy with equation (5.5)

$$\rho_2 = U_2 . \widetilde{\rho_B} . U_2^\dagger \quad \rho_4 = U_{4b} . \widetilde{\rho_B} . U_{4b}^\dagger \tag{5.26}$$

is fulfilled. Index b is used to distinguish the two propagators for the preparation of ρ_4. The experimental implementation of U_2 and U_{4b} is the same as for the U_6 and U_4, only the MW pulses on transitions $|1\rangle \leftrightarrow |3\rangle$ and $|4\rangle \leftrightarrow |6\rangle$ were replaced correspondingly with pulses on $|3\rangle \leftrightarrow |5\rangle$ and $|2\rangle \leftrightarrow |4\rangle$. With this replacement the pulse sequence is the same as in Fig. 5.2. The diagonal elements of the density

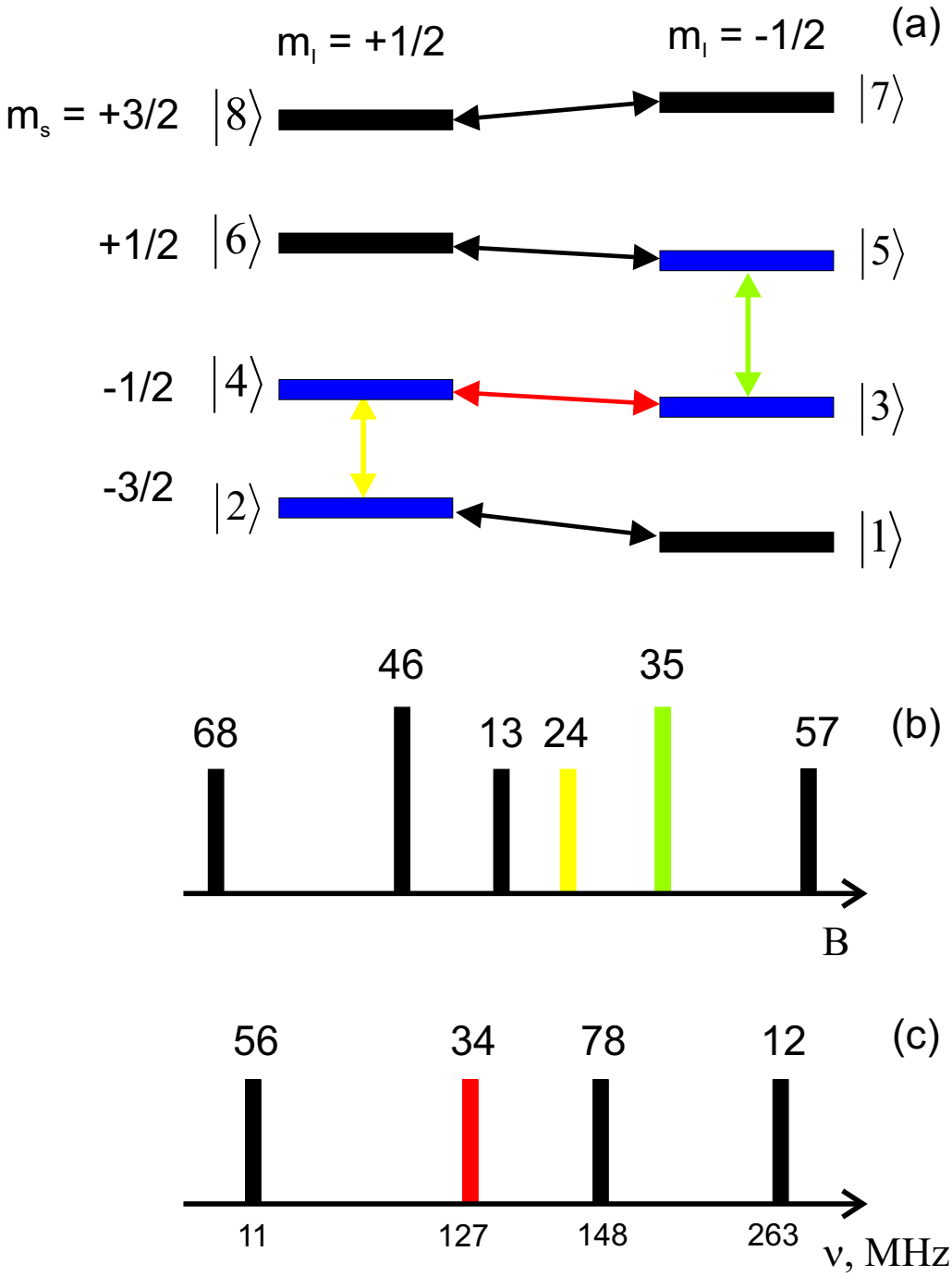

Fig. 5.10: The energy levels of P@C_{60} in BrPOT (a) together with sticks ESR (b) and ENDOR spectra (c). The states of the second subsystem are marked with blue, the ESR transition with green and red and ENDOR transition with red.

matrices ρ_2 and ρ_4 were measured as:

$$\rho_2 = \begin{pmatrix} 1 & 0 & 0 & 0 \\ 0 & 0.02 & 0 & 0 \\ 0 & 0 & 0.02 & 0 \\ 0 & 0 & 0 & -0.04 \end{pmatrix} \rho_4 = \begin{pmatrix} -0.05 & 0 & 0 & 0 \\ 0 & 0.9 & 0 & 0 \\ 0 & 0 & 0.1 & 0 \\ 0 & 0 & 0 & 0.04 \end{pmatrix} \tag{5.27}$$

The next experiment entangles the states $|4\rangle$ and $|5\rangle$ which have equal $|m_s|$ in contrast with the previous entanglement with the hope that its lifetime will be longer. The unitary transformations are defined in complete analogy with equations (5.19) and (5.20):

$$\rho_{ent}^{45} = U_{ent}^{45} . \rho_4 . (U_{ent}^{45})^\dagger \tag{5.28}$$

where '45' denotes the states between which the entanglement is prepared and the propagator is:

$$U_{ent}^{45} = e^{-i\frac{\pi}{2}I_x^{34}} e^{-i\pi S_x^{35}} \tag{5.29}$$

The detection of the entanglement is performed with the back transformation:

$$U_{BT} = P_{\phi_2}^{35}(\frac{\pi}{2}) P_{\phi_1}^{34}(\pi) = e^{-i\phi_1 S_z^{35}} e^{-i\pi S_x^{35}} e^{-i\phi_1 S_z^{35}} e^{-i\phi_1 I_z^{34}} e^{-i\frac{\pi}{2}I_x^{34}} e^{i\phi_1 I_z^{34}} \tag{5.30}$$

The experimental implementation is a pulse sequence very similar to the one depicted in Fig. 5.7 and for convenience is shown in Fig. 5.11.

Surprisingly, the entanglement between $|4\rangle$ and $|5\rangle$ could not be so well prepared

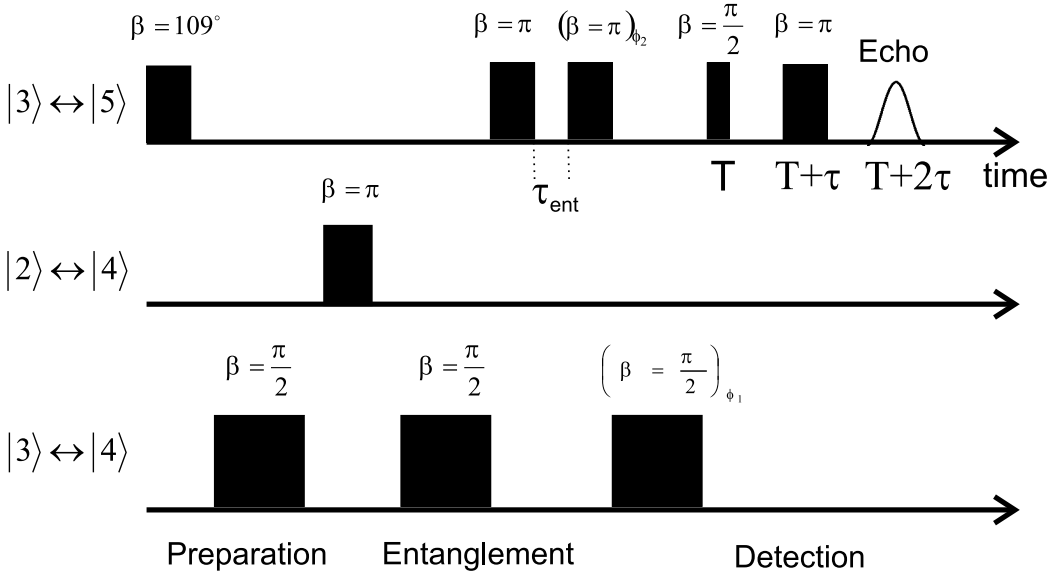

Fig. 5.11: Pulse sequence for the entanglement ρ_{ent}^{45}

as ρ_{ent}^{14} no matter the optimization of the pulse lengths and the variations of τ_{ent}.

In the Fourier transform of the phase oscillations the peaks of the individual spin phase frequencies were comparable with the peak of their sum (the entanglement peak). The best achieved result with fidelity $F = 0.462$ is shown in Fig.5.12. A

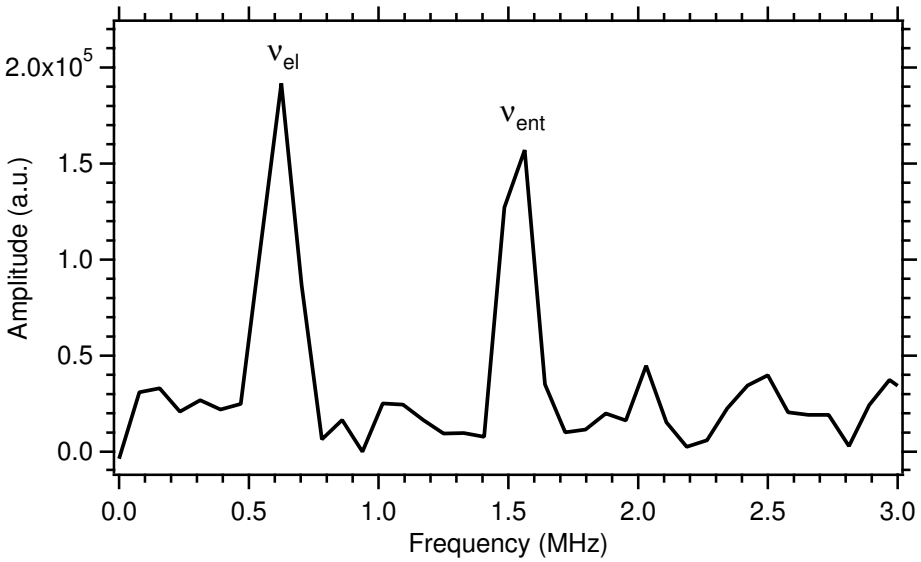

Fig. 5.12: The best result for the preparation of the entanglement between $|4\rangle$ and $|5\rangle$. The peak at the electron spin phase rotation frequency $\nu_E = 625$ kHz is seen together with a peak at $\nu = \nu_I + \nu_E = 1.525$ MHz with almost equal intensity. The fidelity is $F = 0.462$.

possible explanation of the poor quality of the prepared entanglement could be that its lifetime is so short that it is already destroyed before the back transformation pulse sequence is applied. However, it is still unclear why the coherence time is so short.

To measure quantitatively the decay of the previously well prepared entangled state the following experiment was performed. First states $|2\rangle$ and $|3\rangle$ were entangled as in the case of ρ_{ent}^{14}. Then the delay time τ_{ent} was again set to 30 ns and the result obtained for ρ_{ent}^{14} was reproduced. Afterwards in a number of successive experiments τ_{ent} was increased and the entanglement peak in the Fourier transform of the phase oscillation was integrated. The obtained decay is depicted in Fig. 5.13 where the peak areas are normalized to the area of the first peak. From the exponential fit a coherence time $T_2^{ent} = 55 \pm 5$ ns is extracted. The measured usual T_m^{ESR} (the shorter one) is about $12\,\mu$s at this temperature, so obviously the entanglement is much more sensitive to decoherence from the environment than the simple electron coherence time. The possible sources of decoherence will be now discussed. The observed decay of the entanglement can be thought os as its "FID" which can be theoretically refocused but experimentally this is not possible as was discussed in the previous section. The abundant protons in the BrPOT solid state matrix inhomogeneously

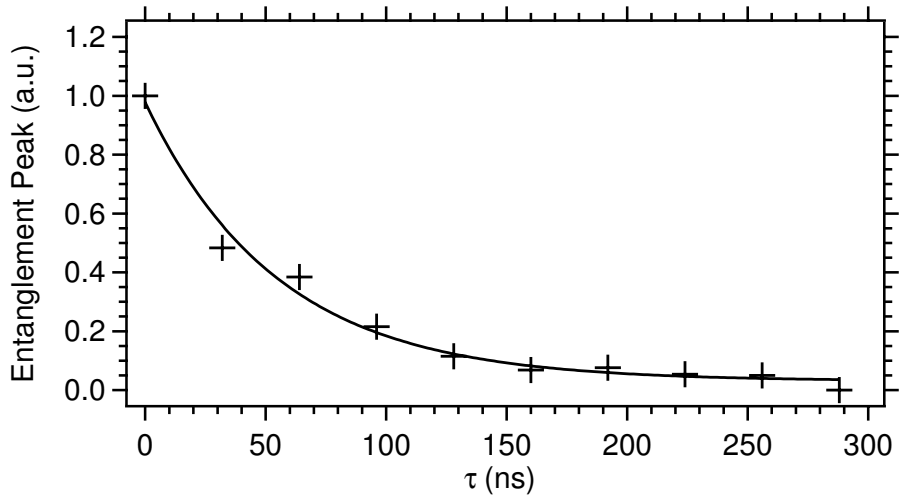

Fig. 5.13: Decay of the entanglement ρ_{ent}^{23}.

broaden the ESR lines so much that no FID could be measured on the ESR transitions when $T_2^* \approx t_d$ where t_d is the spectrometer dead time and $1/(2\pi T_2^*)$ is the line width (see chapter 1.4.4). For comparison, in polycrystalline P@C_{60} and N@C_{60} FIDs with $T_2^* = 5\ \mu$s are readily observed. Moreover, entanglement of two levels with $|m_s| = 3/2$ in ^{15}N@C_{60} [121] shows a coherence time $T_2^{ent} = 207$ ns, about four times longer than T_2^{ent} of BrPOT. Thus it seems that the presence of protons really influences the coherence of the entanglement but the cited experiments were done in X-Band so a direct comparison is not possible. To test whether the protons limit the coherence time of the entanglement, deuterated BrPOT could be synthesized. The latter must be co-crystallized with P@C_{60} from deuterated toluene solution to obtain proton free rhombohedral crystals. Performing relaxation and entanglement experiments with these samples should reveal the role of the protons in the decoherence.

The size of the ZFS is not likely to have great influence on the coherence of entanglement. In N@C_{60} there is some small ZFS $D = 0.52$ MHz at lower temperatures [58] which is about 80 times smaller than the ZFS used in the experiments with P@C_{60} in BrPOT while for the entanglement in both systems $\tau_{ent}^{N@C_{60}} \approx 4\tau_{ent}^{P@C_{60}}$ is fulfilled. Actually the relaxation rate of the entanglement $1/\tau_{ent}^{P@C_{60}} = 18$ MHz is not comparable with any of the spin interactions in this systems like hyperfine constant $a = 137$ MHz, ZFS $D = 120$ MHz and coupling to the neighboring protons $a_H = 200$ kHz. So the real reason for the observed fast decoherence is still unknown, but experiments with deuterated samples could provide more information.

5.5 Conclusions

Pseudo-pure states were prepared in a subsystem of four levels in P@C_{60} in BrPOT at $T = 25$ K in W-band. Density matrix tomography was performed using Rabi oscillations to measure the diagonal elements of both prepared pseudo-pure states. The latter differ from the theoretically expected density matrix by only a few percent, probably because of pulse imperfections.

Pseudo-entanglement between different states was experimentally created and detected using phase oscillations. The lifetime of the entanglement was found to depend on the states involved. States with $|m_s| = 1/2$ could not be fully entangled in contrast to the case when one of the states has $|m_s| = 3/2$. The coherence time of the latter entanglement was measured to be $T_2^{ent} = 55 \pm 5$ ns, a value much shorter than the electron spin coherence time $T_2 = 17$ μs. The strong decoherence is still puzzling and can only partially be attributed to the coupling of the endohedral atom to the abundant protons in the BrPOT matrix. The created coherence (entanglement) between the states of the subsystem might be transferred to the surrounding protons. T_2^{ent} of bulk N@C_{60} is about four time larger than of P@C_{60} in BrPOT, hence these protons indeed cause decoherence.

For coherence time $T_2^{ent} = 55$ ns and typical gate time (duration of the MW pulse) of $t_{gate} = 50$ ns the theoretical number of operations $N_{gate} = 1$ is estimated. Moreover, in this system RF pulses with typical length of 50 μs must be used, so N_{gate} decreases to 10^{-3}. Obviously there is no practical use of such a system for quantum computation, but the performed experiments show how sensitive are the entangled states to decoherence. Entanglement of P@C_{60} in deuterated BrPOT could possibly increased coherence time. Another possibility would be to decouple the protons in the BrPOT from the endohedral atom. Encapsulation of doubly filled dimers like P@C_{60}-P@C_{60} in BrPOT could allow the entanglement of endohedral electrons from two different cages.